Quantum study of the CH_3^+ photodissociation in full dimension Neural Networks potential energy surfaces

Pablo del Mazo-Sevillano,[1] Alfredo Aguado,[1] Javier R. Goicoechea,[2] and Octavio Roncero[2, a)]
[1)] *Unidad Asociada UAM-IFF-CSIC, Departamento de Química Física Aplicada, Facultad de Ciencias M-14, Universidad Autónoma de Madrid, 28049, Madrid, Spain*
[2)] *Instituto de Física Fundamental (IFF-CSIC), C.S.I.C., Serrano 123, 28006 Madrid, Spain*

(Dated: 24 April 2024)

CH_3^+, a cornerstone intermediate in interstellar chemistry, has recently been detected for the first time by the James Webb Space Telescope. The photodissociation of this ion is studied here. Accurate explicitly correlated multi-reference configuration interaction *ab initio* calculations are done, and full dimensional potential energy surfaces are developed for the three lower electronic states, with a fundamental invariant neural network method. The photodissociation cross section is calculated using a full dimensional quantum wave packet method, in heliocentric Radau coordinates. The wave packet is represented in angular and radial grids allowing to reduce the number of points physically accessible, requiring to push up the spurious states appearing when evaluating the angular kinetic terms, through a projection technique. The photodissociation spectra, when employed in astrochemical models to simulate the conditions of the Orion Bar, results in a lesser destruction of CH_3^+ compared to that obtained when utilizing the recommended values in the kinetic database for astrochemistry (KIDA).

I. INTRODUCTION

The long-sought-after CH_3^+ cation has been recently detected for the first time in a protoplanetary disk (d203-506) illuminated by the strong far ultraviolet (FUV) radiation field from nearby massive stars in Orion's Trapezium cluster[1]. This detection was only possible in the infrared, through vibrational spectroscopy, at ≈ 1400 cm^{-1}, within the PDRs4All program using the James Webb Space Telescope (JWST). This highly symmetric cation, with a planar D_{3h} configuration, has no permanent dipole moment and thus cannot be observed through microwave rotational spectroscopy. On the contrary, the rotational spectra of its deuterated isotopologues, such as CH_2D^+ or CHD_2^+, has been experimentally characterized[2–4], but only a tentative detection of CH_2D^+ has been reported so far[5].

Hydrides are the first molecules to form in the interstellar medium (ISM) and provide crucial information on the physical conditions, such as the cosmic-ray ionization rate and H_2/H abundance ratios[6]. The precise determination of their abundances is key to the following chemistry in the ISM. Carbon hydrides are of paramount importance because the allotropy of carbon triggers the molecular complexity in space: from organic and prebiotic molecules, to polycyclic aromatic hydrocarbons (PAH's), amorphous carbon and many different minerals. CH_n^+ cations are particularly important because ion-molecule reactions are typically faster and the low ionization energy of carbon (11.3 eV), below that of hydrogen (13.6 eV), produces high C^+/C abundance ratios in molecular gas irradiated by FUV (6 eV $<$ E $<$ 13.6 eV).

Carbon cations present very anomalous properties, giving rise to the development of the field of the carbocation chemistry[7,8], where the spectroscopic characterization of these species, pioneered by Takeshi Oka[9–12], plays an important role not only in astrochemistry but also in combustion chemistry.

The smallest CH^+ carbocation is formed in C + H_3^+ or C^+ + H_2 reactions. The reaction C^+ + H_2 is endothermic by ≈ 0.5 eV[13], but it becomes exothermic for vibrationally excited $H_2(v > 1)$[14]. It is known that enhanced abundances of FUV-pumped vibrationally excited H_2 significantly increase the reactivity of H_2 in FUV-irradiated molecular clouds[15–17], so-called photodissociation regions (PDRs). Indeed, observations of PDRs reveal the presence of vibrationally excited H_2 up to $v = 12$ in several interstellar PDR's[18,19]. The use of quantum state-to-state rate constants in chemical formation and excitation models applied to the formation of CH^+ describes very well the observed rotational emission lines detected in PDRs[20,21].

Once CH^+ is formed, the successive addition of hydrogen atoms occurs via reactive collisions with H_2, in exothermic or nearly thermoneutral reactions of the type $H_2 + CH_n^+ \rightarrow H + CH_{n+1}^+$. This sequence stops at CH_3^+, because the reaction H_2 + CH_3^+ is very slow and no CH_4^+ products are observed in several experiments[22–24]. The reaction to form the floppy methane cation[25,26], CH_4^+, is endothermic and is not expected to be formed in this hydrogenation sequence. Instead, CH_4^+ is probably formed from neutral CH_4 by photoionization or electron impact, and this cation can react again with H_2 to form CH_5^+[27], a very floppy cation whose infrared spectra have been widely studied[11,28,29].

The relative stability of CH_3^+ with H_2 makes this cation play an important role in the formation of more complex molecules[30–32]. The deuteration of CH_3^+ is relatively

[a)]Electronic mail: octavio.roncero@csic.es

fast[22–24] and its deuterated isotopologues are considered to be determinant in the gas phase formation of complex deuterated molecules, whose observed abundance is several orders of magnitude higher than expected based on the cosmic D/H ratio. Moreover, since the rovibrational spectra of CH_3^+ can be observed by JWST, CH_3^+ is expected to be a useful diagnostic to determine the physical conditions of FUV-irradiated environments (from clouds to protoplanetary disks[1,33]).

The vibrational spectroscopy of CH_3^+ has been the subject of many theoretical[34–37] and experimental[9,10,24,38] studies. The photoionization of the neutral methyl radical has also been studied using several techniques[37,39–46], which also gives information of the rovibrational structure of the CH_3^+ cation.

The photodissociation cross sections of CH^+, CH_2^+ and CH_4^+ have been reported previously[47]. However, there is only one study on the photodissociation of CH_3^+ carried out nearly 50 years ago[48], in which vertical excitation was considered from the planar D_{3h} equilibrium geometry on the ground electronic state. It was concluded that the oscillator strength leading to dissociation from the ground electronic state is very low. It is worth mentioning that, in the kinetic data base for astrochemistry (KIDA), the recommended rate constant for the photodissociation of CH_3^+ under the local mean interstellar radiation field is $2 \cdot 10^{-9}$ s^{-1} (see also Ref.[49]). The value of $2 \cdot 10^{-9}$ s^{-1} is rather high according to the previous study[48], and it is therefore important to determine the photodissociation rate of CH_3^+ more accurately.

The objective of this work is to study the photodissociation cross-section of CH_3^+ using quantum full dimension dynamics to properly assess the destruction of this cation under different FUV radiation fields. The work is distributed as follows. In section II the *ab initio* calculations of the first electronic states of CH_3^+ are described. The neural network fitting of the first three electronic states are described in section III. The vibrational bound states of the ground electronic states are described in section IV. The transition dipole moments and their fit are described in section V. The calculation of the photodissociation cross section are described in section VI, and their use in astrochemical models in section VII. Finally, section VIII is devoted to extract some conclusions.

II. ELECTRONIC STATES

The three lower electronic states of CH_3^+ are calculated using the explicitly correlated internally contracted multi-reference configuration interaction (ic-MRCI-F12) method[50,51], with the MOLPRO suite of programs[52] and the cc-pCVTZ-F12 electronic basis set[53]. The molecular orbitals are optimized using the state-averaged complete active space self-consistent field (SA-CASSCF) method, with 7 active orbitals, for the three lower singlet electronic states. Hereafter, the origin of energy is set at the planar D_{3h} equilibrium configuration of the ground state,

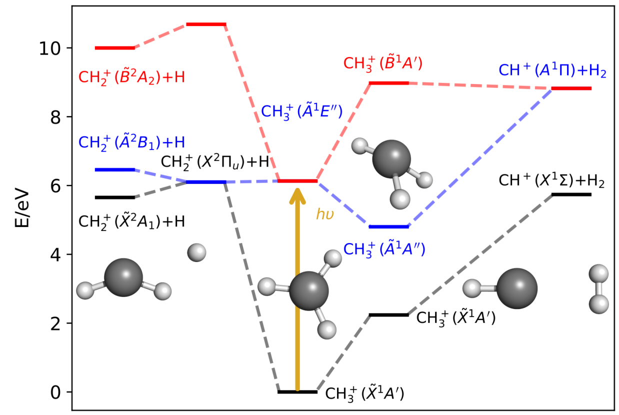

FIG. 1: Energy diagram of the lower electronic states of CH_3^+ obtained with the ic-MRCI-F12 method. The double degenerate $CH_2^+(X^2\Pi_u)$ +H, split in the bent $\tilde{X}$ and $\tilde{A}$ states, produced by a strong Renner-Teller interaction. Black, blue and red lines refer to the ground, first and second excited electronic states, respectively

with a C–H distance of 1.0892 Å, in very good agreement with previous calculations[34,35,48,54]. An energy diagram of the three first electronic states is shown in Fig. 1.

The ground electronic state correlates adiabatically with the $CH_2^+(\tilde{X}^2A_1)$ + H and $CH^+(X^1\Sigma^+)$ + H_2 asymptotes, which are both located at ≈ 6 eV over the equilibrium configuration. The ground and first excited electronic states tend to the linear $CH_2^+(X^2\Pi_u)$ + H fragments, presenting a Renner-Teller interaction. The path towards the formation of CH^+ + H_2 can be seen as a subsequent step after the formation of CH_2^+ + H, where the H approaches one of the CH_2^+'s hydrogens, which is in an almost linear configuration. The C–H bond breaks while the H–H forms towards the CH^++H_2 geometry. Due to the proximity of these geometries to the CH_2^+ linear configuration, the process occurs close to a conical intersection (CI). The first adiabatic excited electronic states does not lead to CH^+ in the ground $X^1\Sigma^+$ state but in the excited $A^1\Pi$, a degenerate state towards which the second excited state also correlates.

Considering a vertical excitation, the first electronic state corresponds to the double degenerate $^1E''$, at the highly symmetric geometry of the ground equilibrium geometry, as reported previously[48,54]. The next excited states in the Franck-Condon region, the $^1A_2''$ and $^1E'$, are ≈ 13 eV higher, close to the atomic hydrogen ionization and are not expected to contribute significantly.

The cuts of the potential along the normal coordinates of the ground state are shown in Fig. 2. These normal modes are in good agreement with previously reported ones[48,54] and correspond to the singly degenerate states, ν_1, the symmetric stretching, and ν_2, the umbrella vibration, and two degenerate vibrations, ν_3 and ν_4. The elon-

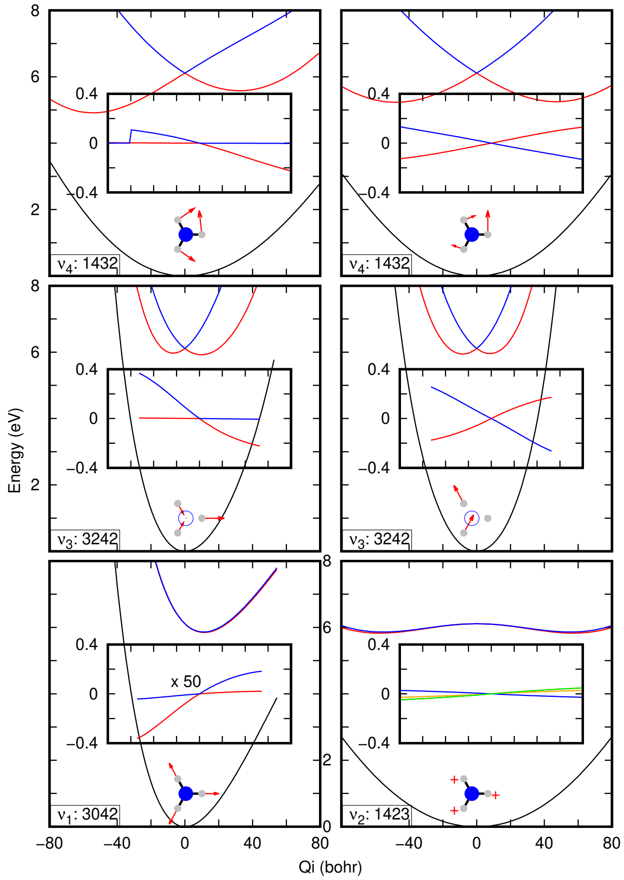

FIG. 2: Mono dimensional cuts along the normal modes, Q_i, of the CH_3^+ (at the planar D_{3h} equilibrium geometry of the ground electronic state) for the lower three electronic states calculated at ic-MRCI-F12 level of theory. In each panel, the boxed inset corresponds to the transition electric dipole moment for the $\tilde{X} - \tilde{A}$ and $\tilde{X} - \tilde{B}$ transition (in atomic units) for the non-zero Cartesian components (at equilibrium the molecule is in the x-y plane). For normal modes 2-6 only the z component is non-zero and red and blue lines correspond to the $\tilde{X} - \tilde{A}$ and $\tilde{X} - \tilde{B}$ transition dipole moment. For normal mode 1, the x, y components of d_{XA} and d_{XB} are represented by red, orange, blue and green lines, respectively . The other inset is a graphical representation of each normal mode. The energy of each normal mode is also indicated, in inverse centimeters.

gation of the normal coordinates for ν_2 and ν_1 remains in the C_{3v} and D_{3h} symmetry, respectively, and the two excited electronic states remain degenerate. This degeneracy is broken along the degenerate vibrations, ν_3 and ν_4, showing the typical CI behavior of the Jahn-Teller effect, with the seam at the configuration of highest symmetry.

III. NEURAL NETWORK POTENTIAL ENERGY SUFACES FITTING

New analytical full dimensional potential energy surfaces (PESs) have been developed to describe the three lower adiabatic electronic states of CH_3^+. A fundamental invariant neural network (FI–NN)[55] takes into account the exact permutation symmetry of the three hydrogen atoms. Three FI–NN are trained –one for each of the three adiabatic energies. While a single FI–NN could handle the calculation of the three electronic states, this setup provides more flexibility in order to make use of the most accurate PESs for different tasks: vibrational state calculation in the ground electronic state and quantum dynamics in the excited states. Moreover, the data from the third excited state tends to be noisier due to interactions with higher excited states, what could interfere with the training process.

In all cases, the multilayer perceptron (MLP) architecture is used, which involves two hidden layers with 50 neurons each. Hyperbolic tangents are used as activations between the hidden layers. The input features are represented by fundamental invariants (FI) of the $p_{ij} = \exp(-\alpha \cdot d_{ij})$ functions, with $\alpha = 0.5\ a_0^{-1}$ and d_{ij} the interatomic distance between atoms i and j. There is a total of nine FI for the A_3B case, which expressions are provided elsewhere[56]. The mathematical expression of the MLPs is the standard one, where the values of the ith neuron in the $(l+1)$ layer are computed through those from the previous layer and a trainable set of weights ($\boldsymbol{w}$) and bias ($\boldsymbol{b}$). σ represents the activation function —the hyperbolic tangent or linear function.

$$H_i^{(l+1)} = \sigma\left(w_{ij}^{(l)} H_j^{(l)} + b_i^{(l)}\right) \tag{1}$$

The MLPs are trained on a set of nearly 25000 energies computed at a ic-MRCI-F12/cc-pCVTZ-F12 level of theory with MOLPRO 2012. An extra set of about 5000 energies is left as test set. A total of ten models are trained, but only the one which better performs on the test set is used. Building this energy dataset is performed in an iterative process, which starts with a rather small set of geometries computed from normal mode displacements of equilibrium geometries and then includes data from minimum energy paths or quantum and classical dynamics on intermediate fits of the system. These fits are done up to 15 eV and 25 eV for the two first and third electronic states, respectively.

The training process is similar to those previously described for H_4^+ and OH + H_2CO systems[57,58] and is performed with an in-house Python code based on PyTorch library[59]. An L-BFGS optimizer[60] is used and the loss function is the Mean Square Error (MSE) error of the predicted energies compared with the ic-MRCI-F12/cc-pCVTZ-F12 energies:

$$\mathcal{L} = \frac{1}{N}\sum_{i=1}^{N} (E_i - E_i^*)^2 \tag{2}$$

E < /eV	State $\tilde{X}$	State $\tilde{A}$	State $\tilde{B}$
1.0	26.2 (461)	–	–
5.0	46.5 (5960)	43.8 (391)	–
10.0	131.3 (17657)	92.7 (13428)	135.5 (7528)
15.0	355.8 (24998)	91.4 (24803)	150.2 (23230)

TABLE I: RMSE for the PES of the three electronic states. The errors are presented in meV. In parenthesis the number of geometries in the energy range.

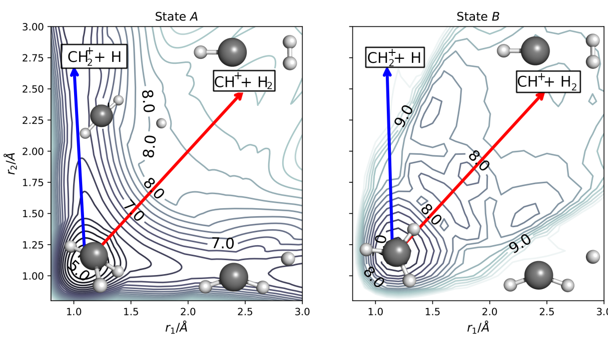

FIG. 3: Contour plot of the PES for the $\tilde{A}$ and $\tilde{B}$ electronic states in terms of the heliocentric Radau coordinates r_1 and r_2. All the other coordinates are relaxed to the minimum energy configuration. The energies are represented in eV.

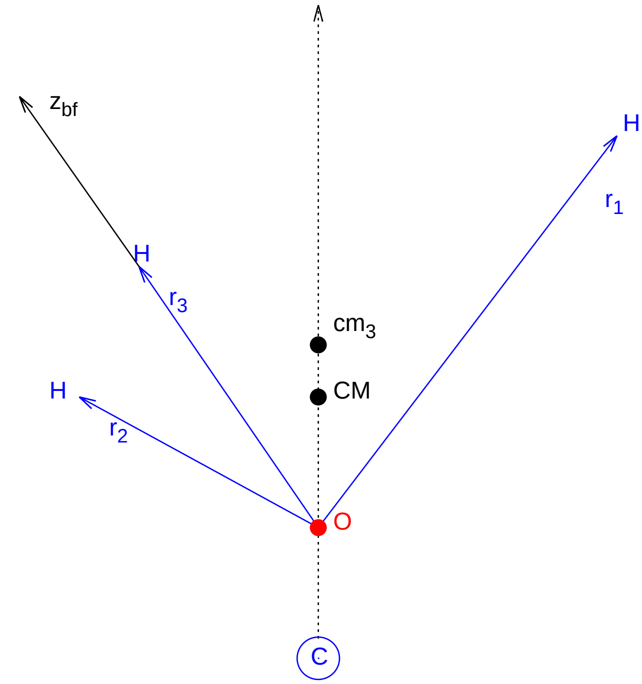

FIG. 4: Graphical description of the heliocentric Radau coordinates used in this work. CM and cm_3 are the center-of-mass of CH_3^+ and the H_3 subunit, respectively. The origin O is defined as in Ref.[61] to eliminate kinetic crossing terms in the kinetic energy operator.

where N is the total amount of training data and E_i is the ith energy. The asterisk indicates *ab initio* energy.

The Root Mean Square Error (RMSE) of the three PES is presented in table I for several energy ranges. The errors are shown in meV units. The PES for the $\tilde{X}$ state remains accurate up to electronic energies of 6–7 eV, enough to compute highly accurate vibrational states. The PESs for the $\tilde{A}$ and $\tilde{B}$ states remain accurate up to higher electronic energies, although the latter presents larger errors, in part due to the difficulty to converge the *ab initio* calculations for this state, which interacts with higher excited electronic states.

In the following we analyse in more detail the $\tilde{A}$ and $\tilde{B}$ states. Fig. 3 presents the relaxed PES over two radial coordinates r_1 and r_2, using heliocentric Radau coordinates as defined below. For the $\tilde{A}$ state there is a minimum, corresponding to a CH_3^+ (2^1A). The minimum in the $\tilde{B}$ state is in the Franck–Condon region and corresponds to CH_3^+ $(^1E'')$.

The path to the CH_2^+ + H product occurs in the $\tilde{A}$ state after surpassing a low energy transition state less than 1 eV above the minimum. On the other hand, the path to the CH^+ + H_2 is highly endothermic, ≈ 4 eV over the minimum, with no barrier. The path towards the formation of CH_2^+ + H can be merely explain as a C–H elongation —related to the elongation of the r_i coordinate in Fig 3. The path towards CH^+ + H_2 is not so direct, and proceeds via elongation of one of the C–H distances getting close to a CH_2^+ configuration. After this, the second r_i distance elongates breaking a C–H bond while forming the H_2 molecule. In both cases the minimum energy paths get close to an almost linear configuration of the CH_2^+ —a $^2\Pi_u$ state, degenerate with the ground electronic state— what implies that $\tilde{X}$ and $\tilde{A}$ electronic states get close in energy as the photodissociation process occurs.

Regarding the reactions on the $\tilde{B}$ state we find that both reactions are highly endothermic. The Franck–Condon region becomes the absolute minimum with no other product close in energy as the CH_2^+ + H in the A electronic state. Hence, we do not expect reactivity in this state to be important up to photon energies ≈ 9 eV and ≈ 10 eV for CH^+ + H_2 and CH_2^+ + H respectively. For this reason, we expect the CH_3^+ in the $\tilde{B}$ electronic state to remain mostly bounded for the photon energies of interest in this work.

IV. BOUND VIBRATIONAL STATES

The bound state calculations are done in two steps: first, the eigenvalues are calculated using an iterative non-orthogonal Lanczos method[62], and second, a conjugate gradient method[63,64] is used to obtain the eigenvectors. These procedures are implemented in a parallel MPI form using heliocentric Radau coordinates[35,61,65], illustrated in Fig. 4. Three vectors $\mathbf{r}_i$ are defined, corresponding to the distance of each hydrogen to a center O, situated along the line joining the centers-of-mass of CH_3^+ and H_3. This center O is chosen to make zero the kinetic coupling terms among the vectors $\mathbf{r}_i$, and the Hamiltonian thus built is formally identical to that of Jacobi coordinates[61,65]. A body-fixed frame is chosen, in which $\mathbf{r}_3$ lies parallel to the z-axis, and $\mathbf{r}_1$ is in the $x-z$ body-fixed plane. Thus the coordinates are separated as three external Euler angles, α, β, γ, defining the body-fixed frame, and six internal coordinates r_i $(i = 1, 2, 3)$, θ_j $(j = 1, 2)$ and ϕ. The wave functions, for a given total angular momentum J, are described as

$$\Psi^{JM} = \sqrt{\frac{2J+1}{8\pi^2}} D^{J*}_{M\Omega}(\alpha,\beta,\gamma) \frac{\Phi^{JM}_{\Omega}(r_1, r_2, r_3, \theta_1, \theta_2, \phi)}{r_1 r_2 r_3}, \tag{3}$$

where $D^{J*}_{M\Omega}$ are Wigner rotation matrices[66], with M and Ω being the projections of the total angular momentum $\mathbf{J}$ on the space-fixed and body-fixed frames respectively.

The internal coordinates are described in grids. Sinc Discrete Variable Representation (DVR)[67] is used to describe the radial r_i coordinates, non-orthogonal Gauss-Legendre DVR[68,69] to describe θ_i, and equispaced points in the interval $[0, 2\pi]$ to describe ϕ. The evaluation of each kinetic term is done by transforming to finite basis representation (FBR), where it is analytical. This transformation is done sequentially, one internal coordinate by one, to save computation time as it is done in other approaches representing the wave function in the FBR and then transforming sequentially to the DVR to evaluate the potential[70,71].

Representing the wave functions in grids for internal coordinates has the advantage of saving many points, the so called L-shaped grids[72], thus reducing considerably the memory and time requirements of the calculations. However, the numerical sequential method done to transform from DVR to FBR, usually introduces spurious states when evaluating the rotational kinetic terms using finite DVR grid points. To avoid this problem, we have developed a projection method to move the spurious states up, out of the physical energy interval of interest, as described in the appendix.

The bound state calculations are done using a grid of 20 DVR points in the radial coordinates, r_i, in the interval $[0.5, 1.6793]$ Å, 30 Gauss-Legendre points for θ_i, and 61 points in ϕ. About 10^4 Lanczos iterations were done to converge the eigenvalues.

Fig. 5 shows the cuts of the density probability associated to some bound states; those corresponding to the ground and first excitation on each mode (ν_1, ν_2, ν_3, ν_4) for total angular momentum $J = 0$. Their energies are tabulated in Table. II. The heliocentric Radau coordinates are well adapted to describe the permutation symmetry of the hydrogen atoms, but in this first implementation no symmetry–adapted basis functions or grids are used. For the degenerate modes (ν_3 and ν_4) only one case is shown.

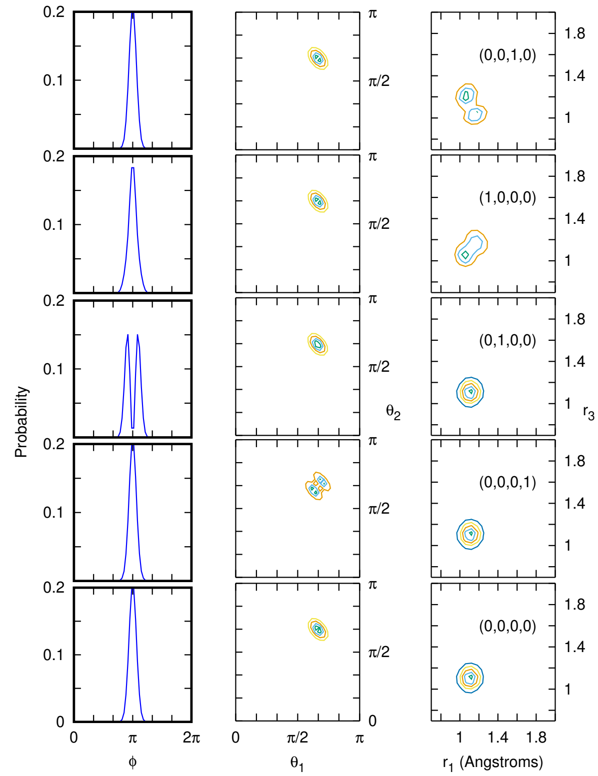

FIG. 5: Cuts of the density probabilities associated to different bound states of $CH_3^+(\tilde{X})$, denoted by the the vibrational modes (ν_1, ν_2, ν_3, ν_4). These bound states correspond to the the energy levels 1, 2, 3, 7 and 8.

TABLE II: Lowest excitation energies (in cm^{-1}) for the vibrational modes of CH_3^+, obtained as described in the text for $J = 0$. The zero-point energy of the ground rovibrational state is 6776.898 cm^{-1}.

vibrational mode	This work	Ref.[34]	Ref.[37]
ν_1	2947.82	2949.8	2943.43
ν_2	1424.53	1432.5	1405.72
ν_3	3113.50	3091.3	3109.06
ν_4	1393.91	1399.3	1394.98

The lowest eigenvalues for each vibrational mode corresponding to the bound states in the ground electronic state are listed in Table II, together with other theoretical values for comparison. The values of Ref.[37] were obtained to simulate the rovibrational spectra observed in the d203-506 protoplanetary disk and experimental data. The present results are within 5 cm^{-1} accurate with respect to those previously reported[34,35,37], except for the ν_2 mode, which deviates $\approx$ 20 cm^{-1}. Previous calculations are based on local fits for the potential, thus describing only the bound states. In this work, however, the potential energy surfaces are global, *i.e.*, they are built to describe the bound states and the fragmentation regions towards the $CH^+ + H_2$ and the $CH_2^+ + H$ products.

For these reasons, we consider this new PES as accurate enough to describe the photodissociation dynamics, with nearly spectroscopic accuracy.

V. TRANSITION DIPOLE MOMENTS

The transition dipole moments required for the $\tilde{X}-\tilde{A}$ and $\tilde{X}-\tilde{B}$ electronic excitation are calculated with MOLPRO programs[52], and to avoid the randomness of the phase of adiabatic eigenvectors, a biorthogonal transformation is used between consecutive points along lines. The Cartesian projections of the transition dipole moments are also shown, in the boxed inset in Fig. 2, for the $\tilde{X}-\tilde{A}$ and $\tilde{X}-\tilde{B}$ excitations, with the molecule being in the $x-z$ plane for the equilibrium geometry. In all cases, the transition dipole moments are zero at $Q_i = 0$, corresponding to the equilibrium geometry. Only ν_2 corresponds to a motion out of the plane of the planar D_{3h} geometry, and it is the only one to have non zero components in x, y and z axis. For the rest of the normal modes, only the component y, perpendicular to the plane of the molecule, is non-zero. This transition dipole moment corresponds to a transition between two of the bonding orbitals of the C^+ atom (mostly corresponding to a sp^2 hybridization) to an unoccupied p_y orbital, out of the plane[54]. As a consequence of the CI of the $\tilde{A}$ and $\tilde{B}$ excited states in D_{3h} geometries[73], there is a sign change of the real electronic part of the wave function under a 2π rotation in the vibrational coordinates, a special case of Berry's geometrical phase.[74–76]

The three components of both transition dipole moments have been fitted to an analytical function, based on mono–dimensional grids for each internal heliocentric Radau coordinates. The fits are localized in the CH_3^+ ($\tilde{X}$) well, switching to zero outside this region. There is no general method for an accurate representation of the dipole moment for polyatomic molecules, using an appropriate functional form. Because the dipole moment is a vector property, its fit is more complicated than that for the energies[73]. One alternative is to use a diabatic representation where the dipole moment is diagonal. In this work we are interested in fitting the adiabatic transition dipole moments between the $\tilde{X}^1A_1'$ ground electronic state and the excited $\tilde{A}$ and $\tilde{B}$ ($^1E''$) states.

The phase of the adiabatic transition dipole moment $\mu_{ij} = \langle\phi_i|\hat{\mu}|\phi_j\rangle$ is arbitrary, because it depends on the phase of the electronic wavefunctions ϕ_i and ϕ_j. In addition, the adiabatic representation becomes inadequate near CIs[73], because real-valued adiabatic electronic wavefunction changes sign when transported around a CI (geometric or Berry phase)[75,76]. In order to make the transition dipole moment continuous, we have calculated the overlap of each electronic state with the same electronic state at a reference geometry –the equilibrium geometry of the ground $^1A_1'$ electronic state– using the biorthogonalization method as programmed in MOLPRO program[52]. The signs of ϕ_i and ϕ_j are corrected in order to make the overlap positive, and then corrects the phase of μ_{ij}. Therefore, in the adiabatic approximation we have not taken into account this change of sign of real electronic wave functions that produces a change of sign of the transition dipole moment when the conical intersection is surrounded in nuclear configuration space.

Once corrected the sign, in order to fit the transition dipole moment, we have expanded each component of the dipole moment as a function of symmetry coordinates of the D_{3h} point group, defined in terms of the Heliocentric Radau coordinates defined above as

$$\begin{aligned}
S_1 &= \Delta r_1 + \Delta r_2 + \Delta r_3 \\
S_2 &= \Delta r_1 - \Delta r_2 \\
S_3 &= 2\Delta r_3 - \Delta r_1 - \Delta r_2 \\
S_4 &= \Delta\theta_1 + \Delta\theta_2 \\
S_5 &= \Delta\theta_1 - \Delta\theta_2
\end{aligned}$$

being $\Delta r_i = r_i - r_e$ $(i = 1,2,3)$ and $\Delta\theta_j = \theta_j - \theta_e$ $(j = 1,2)$ the variation with respect to equilibrium values, $r_e = 1.089$ Å and $\theta_e = 2\pi/3$ and where S_6 is selected as the out-of-plane variation $\Delta\phi = \phi - \phi_e$ of the Radau angle with respect to the equilibrium value, $\phi_e = \pi$.

As shown in Fig. 2, the ν_1 stretching mode corresponds to the variation of the S_1 symmetry coordinate, that belongs to the A_1' irrep of the D_{3h} point group. As a consequence, the only non-zero component is the out-of-plane y component, although in this case it is practically zero, and can be discarded. The ν_2 bending mode corresponds to the variation of the out-of-plane coordinate. This mode belongs to the A_2'' irrep of the D_{3h} point group. In this case the non-zero components are the z component for the $\tilde{X}-\tilde{A}$ transition and the x component for the $\tilde{X}-\tilde{B}$ transition. The other modes are degenerated, and corresponds to the E' irrep. ν_3 corresponds to stretching modes, which can be described by S_2 and S_3, while ν_4 correspond to bending modes that are described by S_4 and S_5. In this cases the non-zero component of the transition dipole is the y component.

Since the S_α ($\alpha = 2, ..., 5$) coordinates do not take into account the symmetry properties of the dipole moment with respect to the exchange of two hydrogens, they are antisymmetrized as

$$\widetilde{S}_\alpha = (-1)^s \sqrt[3]{|S_\alpha \cdot P_{13}S_\alpha \cdot P_{23}S_\alpha|}$$

where P_{ij} is the permutation operator for atoms i and j and where s is a phase to take into account the symmetry of each component with respect to permutation of two hydrogens. When the dipole is antisymmetric with respect to the permutation, $(-1)^s$ is obtained as the sign of the maximum value of $S_\alpha, P_{13}S_\alpha$ or $P_{23}S_\alpha$. Finally, each Cartesian component of the transition dipole moment for the transition from $\tilde{X}^1A_1'$ to $(\tilde{A},\tilde{B})^1E''$ states is expanded as a series in this symmetry coordinates $\widetilde{S}_\alpha$

$$\mu_{ij}^{(x,y,z)} = \mu_{ij}^e + \sum_\alpha^6 a_\alpha \widetilde{S}_\alpha$$

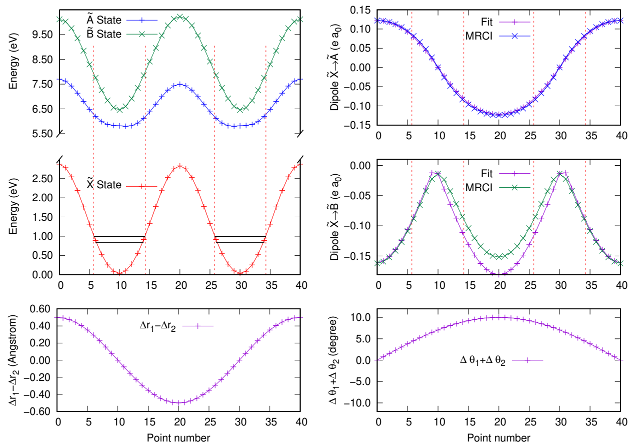

FIG. 6: Transition dipole moment μ^y as a function of the $S_2 = \Delta r_1 - \Delta r_2$ and $S_4 = \Delta\theta_1 + \Delta\theta_2$ symmetry coordinates. The vertical dashed lines defines the Frank-Condon region

with $\mu^e_{ij} = 0$ in this case and where a_α are also developed as a serie

$$a_\alpha = \left(\sum_k^{N_\alpha} a_{\alpha,k} \widetilde{S}_\alpha^k \right) \cdot e^{-b_\alpha \widetilde{S}_\alpha^2}$$

where N_α is the degree of the polynomial, and where the expansion has been multiplied by a Gaussian function in order to avoid extremely large values of the dipole moment in regions very far from the equilibrium position.

In Fig. 6 we show the variation of the transition dipole moment when the symmetry coordinates $S_2 = \Delta r_1 - \Delta r_2$ and $S_4 = \Delta\theta_1 + \Delta\theta_2$ are varied simultaneously, following a sinusoidal movement.

VI. PHOTODISSOCIATION CROSS SECTION

The photodissociation cross section is calculated for each transition with a wave packet method, using the heliocentric Radau coordinate, as described above for the bound state calculations. The modified Chebyshev propagator[77–80] is used to integrate the Schrödinger equation as

$$\begin{aligned} \Phi(k=0) &= \Psi(t=0) \\ \Phi(k=1) &= e^{-\varphi} \hat{H}_s \Phi(k=0) \\ \Phi(k+1) &= e^{-\varphi} \left\{ 2\hat{H}_s \Phi(k) - e^{-\varphi} \Phi(k-1) \right\}, \end{aligned} \tag{4}$$

where $\hat{H}_s = \left(\hat{H} - E_0\right)/\Delta$ is the scaled Hamiltonian, with $E_0 = (E_{max} + E_{min})/2$ and $\Delta E = (E_{max} - E_{min})/2$, E_{max} and E_{min} being the minimum and maximum energy values of the Hamiltonian of the system represented in the grid/basis using in the propagation. The wave packet at time t and eigenfunctions at energy E are expressed in terms of the Chebyshev iterations, $\Phi(k)$, as

$$\begin{aligned} \Psi(t) &= \sum_{k=0}^{\infty} f_k(\hat{H}_s, t) \Phi(k) \\ \Psi(E) &= \sum_{k=0}^{\infty} c_k(\hat{H}_s, E) \Phi(k) \end{aligned} \tag{5}$$

with

$$f_k(\hat{H}_s, t) = (2 - \delta_{k0})\, e^{-iE_0 t/\hbar} \, (-i)^k \, J_k(t\Delta E/\hbar) \tag{6}$$

$$c_k(\hat{H}_s, E) = (2 - \delta_{k0}) \, \frac{\hbar \exp\left[-ik \arccos\{(E - E_0)/\Delta E\}\right]}{\sqrt{\Delta E^2 - (E - E_0)^2}}$$

with J_k being a Bessel function of the first kind.

The absorption cross section is then given by

$$\begin{aligned} \sigma(h\nu) &= \frac{Ah\nu}{\pi\hbar} \mathcal{R} \int_0^\infty dt\, e^{-iEt/\hbar} \, \langle \Psi(t=0) | \Psi(t) \rangle \\ &= \frac{Ah\nu}{\pi\hbar} \mathcal{R} \sum_{k=0}^{\infty} c_k(\hat{H}_s, E) \, \langle \Phi(k=0) | \Phi(k) \rangle \end{aligned} \tag{7}$$

with $A = 1/\hbar^2 \epsilon_0 c$ and $\mathcal{R}$ denoting the real part. For finite propagations (in this case 1000 Chebyshev iterations), the right–hand side of Eq. 7 is multiplied by $\exp(-k\gamma)$, with $\gamma = 10^{-3}$ in the present case.

The wave packet is represented in grids for the internal radial and angular coordinates, using the projection method to shift up the spurious solutions described in the appendix. The angular grids are those used for bound states, while the radial grids are extended to 50 points, keeping the same density of points. The initial wave packet is built for the J_i=0 $\rightarrow$ J=1 transition as described previously[81–83], combining the bound state with the transition dipole moment to the final electronic states, $\tilde{A}$ or $\tilde{B}$, and projecting on a final J. This is done for several bound states with different ν values. The wave packet is propagated about 1000 iterations. At each iteration the autocorrelation function is evaluated, and photoabsorption cross section is obtained by a Chebyshev transformation to the energy domain[80].

In Fig. 7, contour plots of the density probability of the wave packet component, $\Phi(k)$, are shown for the $\tilde{X} - \tilde{A}$ (left panels) and $\tilde{X} - \tilde{B}$ (right panels) transitions, for several values of k

The photoabsorption cross section towards the $\tilde{A}$ and $\tilde{B}$ electronic states are shown in Fig. 8 for different initial vibrational states. To explain the differences between absorption to $\tilde{A}$ and $\tilde{B}$ states, it is important to remind that they present a conical intersection at the Franck-Condon region. Thus, the A state corresponds to a local maximum which tends rapidly to the dissociation limits. One of these limits corresponds to the $CH_2^+(X^2\Pi_u)$ + H products, slightly below the vertical excitation. On the other side, towards the $CH^+(X^1\Sigma^+) + H_2$ products there is an avoided crossing between the $\tilde{X}$ and $\tilde{A}$ state, from which

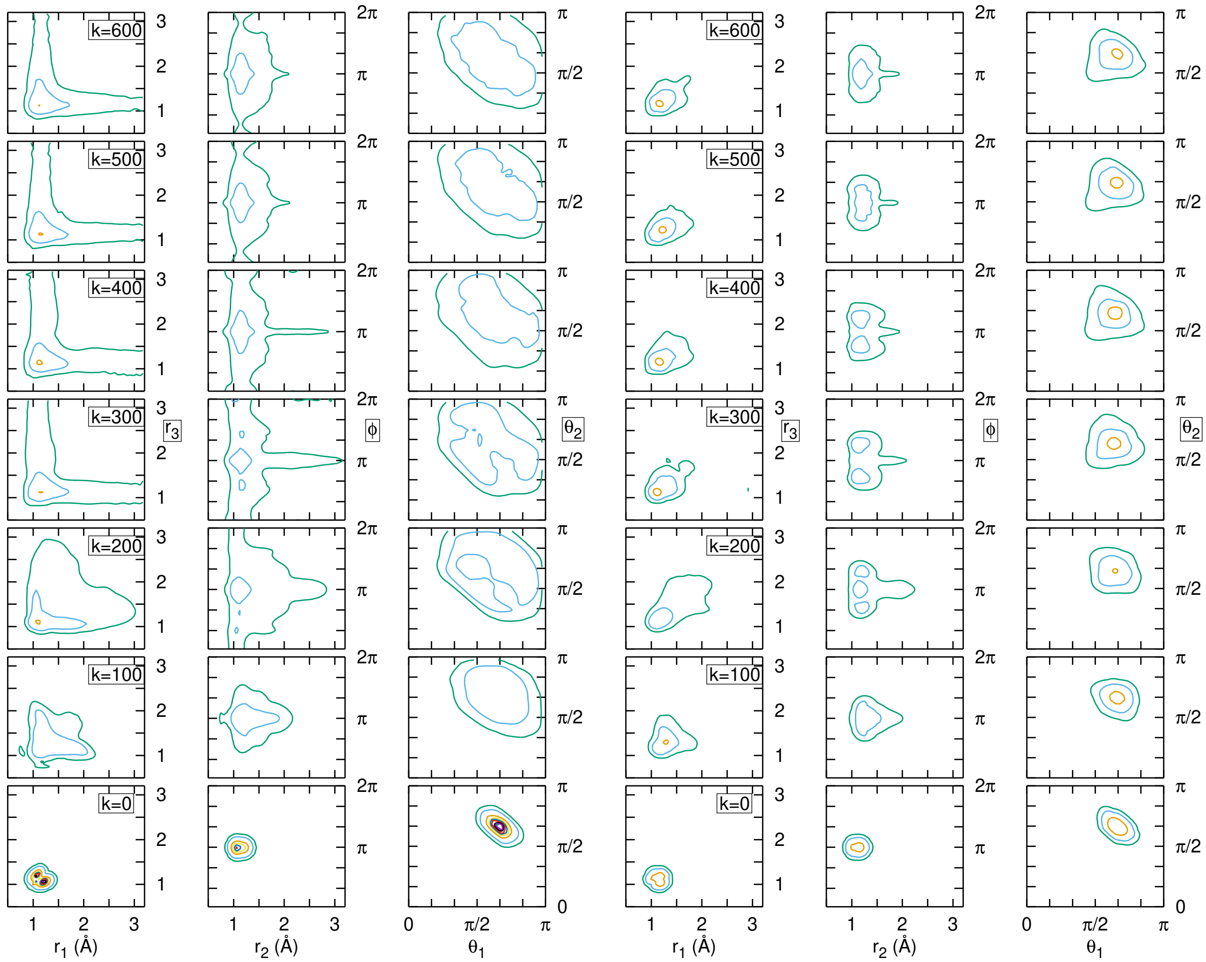

FIG. 7: Cuts of the density probability associated to the wave packet at different iterations k, for the $\tilde{A}$ (left panels) and $\tilde{B}$ (right panels) electronic states, for the transition from the ground electronic and vibrational state.

the potential energy increases monotonically towards the $CH^+(A^1\Pi)$ + H_2 asymptote, at 8.68 eV. The $\tilde{X}-\tilde{A}$ absorption spectrum shows a broad band characteristic of a direct dissociation, mostly below photon energies of 8 eV (corresponding to total energies of 8.84 eV). Clearly, the dissociation must be towards the lower $CH_2^+(X^2\Pi_u)$ + H products, which is also supported by the inspection of the wave packet dynamics and the PESs. The $\tilde{X}-\tilde{A}$ absorption band shows some weak peaks at the lower energies associated to resonances originated by the well around the minimum $CH_3^+(\tilde{A}^1A_1')$ in Fig. 1, which are above the $CH_2^+(X^2\Pi_u)$ + H dissociation limit.

The upper part of the conical intersection, the $\tilde{B}$ state, corresponds to a well, showing dissociation limits at 10.6 eV ($CH_2^+(\tilde{B}^2A_2)$ + H) and 8.68 eV ($CH^+(A^1\Pi)$ + H). Moreover, the PES shows a barrier of $\approx$ 10 eV when elongating one r_i distance towards the $CH_2^+(^2\Pi_u)$ + H products. As a consequence the $\tilde{X}-\tilde{B}$ absorption corresponds to resonant bound–bound transitions, with the wave packet oscillating around the Franck-Condon regions showing many recurrences, mostly at photon energies below 9 eV (*i.e.* at total energies of $\approx$ 9.84 eV). Above this energy, the system can dissociate in the adiabatic $\tilde{B}$ state, what occurs with a low probability. Therefore, most of the wave packet should dissociate by tunnelling at the CI, which tends mainly towards the $CH_2^+(^2\Pi_u)$ + H products.

The spectra of vibrationally excited $CH_3^+(\tilde{X},\ \nu_i$=4,2) shows very similar patterns. The $\tilde{X}-\tilde{A}$ bands for all vibrational states considered are very close, with a shift in the photon energy of ≈ 1400 cm^{-1} (0.174 eV) between the ground and the two excited vibrational states. The $\tilde{X}-\tilde{B}$ spectrum for ν_4 shows a different intensity pattern as compared to that of the ground vibrational, as a result of the excitation on the θ_i angles. However, the $\tilde{X}-\tilde{B}$ for ν_2 gets closer to that of the ground, what is explained

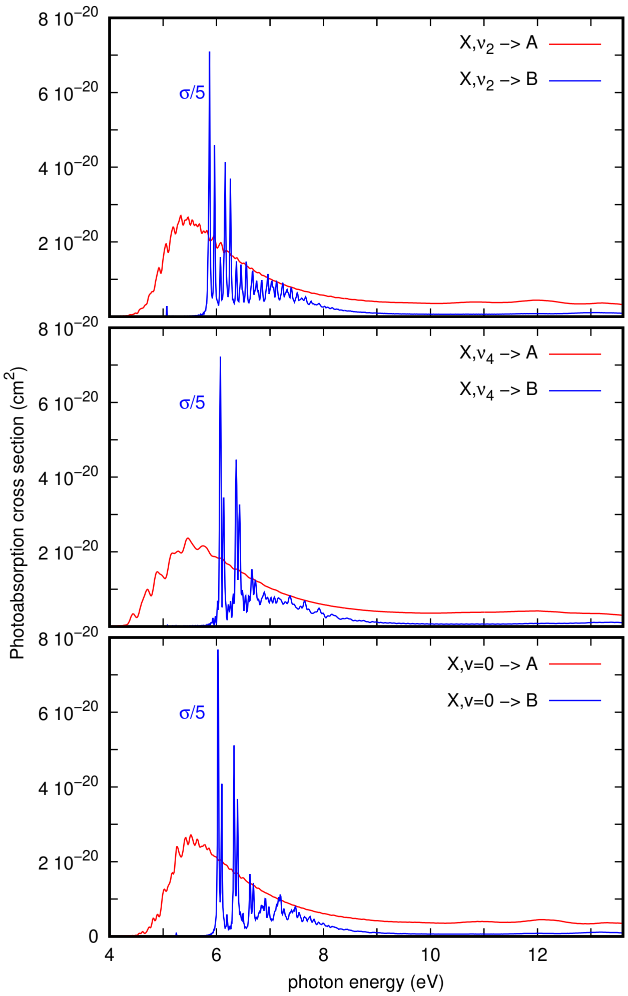

FIG. 8: CH_3^+ photoabsorption cross section (in cm^2) from the ground (bottom), ν_4=1 (middle) and ν_2=1 (top panel) vibrational states towards the excited electronic states $\tilde{A}$ (red) and $\tilde{B}$ (blue), as a function of the photon energy (in eV). The cross section for the $\tilde{X} - \tilde{B}$ transitions have been divided by 5 in the figure.

by the shallower dependence of the potential on the out-of-plane angle ϕ.

VII. ASTROCHEMICAL MODELING

The photodestruction of CH_3^+ in strongly FUV-irradiated objects (such as interstellar PDRs and protoplanetary disks) is determined by the photodissociation rate, *i.e.*, the integral of the photodissociation cross section with energy dependent FUV radiation field. Using Draine's[84] mean interstellar radiation field, the CH_3^+ photodissociation rate is $6.83 \cdot 10^{-12}$ s^{-1}, 7.24 $\cdot 10^{-12}$ s^{-1} and 7.13 $\cdot 10^{-12}$ s^{-1} for the ground vibrational state ($\nu = 0$ in Fig. 8), and for the $\nu_4 = 1$ and $\nu_2 = 1$ excited vibrational states, respectively, with a very minor increase with vibrational excitation of $\approx$ 5-7 %. These values are about 300 times lower than the value of $2 \cdot 10^{-9}$ s^{-1} recommended in KIDA data base. Moreover, KIDA suggests that two photodestruction products, CH_2^+ and CH^+, form at the same rate, while according to this work the only product is CH_2^+ + H.

The photodissociation rate calculated here is rather low, in agreement with the previous estimation by Blint and co-workers[48]. The values reported for CH^+, CH_2^+ and CH_4^+ are $3.3 \cdot 10^{-10}$, $1.4 \cdot 10^{-10}$ and $2.8 \cdot 10^{-10}$ s^{-1}, respectively[47]. These rates are higher than those obtained here for CH_3^+ by a factor of $\approx$ 30. The reason for this is attributed to the "forbidden" nature of the transition dipole moment of CH_3^+ at the equilibrium configuration.

In interstellar clouds strongly illuminated by FUV photons, photoionization of carbon atoms produces a high abundance of electrons, which rapidly recombine with cations, producing excited neutral systems that dissociate. This dissociative recombination (DR) process is very fast, because of the strong Coulomb interactions, of the order of 10^{-7} s^{-1}. Because of the large difference between the photodissociation and DR rates (of about 4 orders of magnitude), it is expected that the destruction of CH_3^+ is dominated by electrons and not by photons.

To show the effect of the photodissociation cross section obtained in this work, and the competition with other processes, Fig. 9 shows an example obtained with the Meudon PDR model[85,86] of a strongly FUV-irradiated molecular cloud, with a FUV radiation field 4×10^4 times the mean interstellar radiation field in the solar neighbourhood, and a constant thermal pressure $P/k_B = n \cdot T = 10^8$ K cm^{-3}. These parameters are appropriate to the Orion Bar PDR, an irradiated rim of the Orion molecular cloud[87]. The upper panel of Fig. 9 shows the predicted gas density, electron density, and temperature profile as a function of depth into the molecular cloud (in magnitudes of visual extinction, A_V). The lower panel shows the resulting abundance profiles, with respect to H nuclei, for the main species discussed in the text. The continuous curves refer to a model that integrates the wavelength-dependent CH_3^+ photodissociation cross-sections determined in this work for the A and B electronic states and leading to CH_2^+ as products. The dashed curve shows a model that uses the CH_3^+ photodissociation rate recommended in KIDA. The dominant process destroying CH_3^+ is dissociative recombination with electrons, thus the two models predict relatively similar abundance profiles. The role of CH_3^+ photodissociation is more clearly seen at the very edge of the PDR, at low A_V, where the flux and energy of FUV photons is high. Here, the model using the recommended rate in KIDA is not realistic and underestimates the CH_3^+ abundance by a factor of about 6. Such difference explains the need of realistic evaluations of the rate constants used in the astrochemical models.

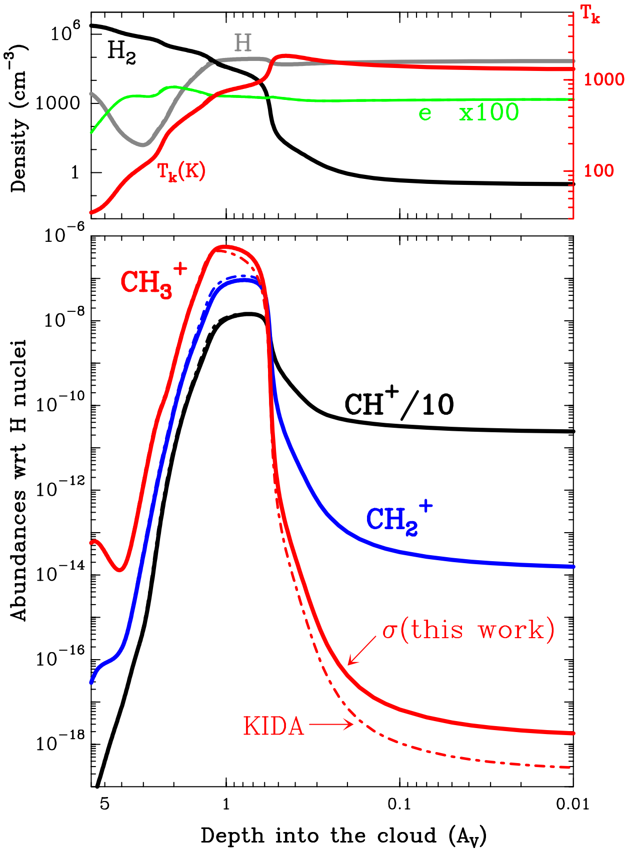

FIG. 9: Results obtained with the Meudon PDR model using physical conditions corresponding to the Orion bar, as a function of FUV shielding or visual extinction parameter A_V (low A_V corresponds to the irradiated rim of the molecular cloud, while high A_V correspond to distances well inside the molecular cloud with low FUV photon flux). Lower panel: abundance ratio (with respect to H) of CH_n^+ fractional abundances (n=1, 2 and 3), using the present CH_3^+ photodissociation rate (solid line) and that of KIDA data base (dashed lines). In the present case, the sum of $\tilde{X}-\tilde{A}$ and $\tilde{X}-\tilde{B}$ photodissociation absorption yields to CH_2^+ products, as described in the text. Upper panel: Evolution of temperature and densities of H, H_2 and electrons and gas temperature as a function of A_V.

VIII. CONCLUSIONS

A quantum treatment is developed to study the photodissociation of the CH_3^+ cation below 13.6 eV. Accurate full dimension PESs are generated using a FI-NN method for the three lower electronic states based on ic-MRCI-F12/cc-pCVTZ-F12 *ab initio*. The transition dipole moments are also fit locally in the region around the equilibrium configuration covering the vibrational bound states in the ground electronic state.

The bound states and wave packet dynamics are studied using heliocentric Radau coordinates, well adapted to account for the permutation symmetry of the three hydrogen atoms. A full grid representation of the internal (radial and angular) coordinates is implemented, allowing saving of memory and computation time due to the L-shape method that allow to discard the grid points with high energy out of the energy range of physical interest. To do so, it was found necessary to apply a projection method to push up the spurious states appearing when evaluating the angular kinetic terms using a sequential transformation from a non-direct DVR basis set to the FBR representation. This is implemented in the home made MadWave4 code, a MPI parallel code written in Fortran.

The calculated bound eigenvalues in the ground electronic states are in good agreement with previous theoretical and experimental ones. The photodissociation cross section from several initial vibrational states towards the excited $\tilde{A}$ and $\tilde{B}$ electronic states have been calculated using a quantum wave packet method. The initial vibrational excitation has little influence in the photodissociation dynamics and the calculated photodissociation rate is about 300 times lower than the recommended one in the KIDA data base for astrochemistry.

The possible fragmentation products in the adiabatic representation is mostly towards the CH_2^++ H products for the $\tilde{A}$ state. On the $\tilde{B}$ electronic state, however, most of the absorption spectrum corresponds to the bound region, and without including non-adiabatic transitions the wave packet cannot yield to dissociation. It is considered that this bound wave packet could be trasferred to the $\tilde{A}$ state, where it can dissociate. A diabatization of the electronic Hamiltonian is being done to consider the non-adiabatic transitions needed to a proper description of the branching ratios. This is left for a future work

The effect of the calculated cross section in interstellar regions strongly illuminated by FUV photons is analyzed using the Meudon PDR code applied to the Orion Bar as a prototype. It is found that the dominant destruction mechanism of CH_3^+ is the dissociative recombination with electrons, and that the use of the KIDA photodissociation rate underestimates the CH_3^+ abundance, demonstrating the need of realistic evaluation of rate constants in astrochemical models.

IX. SUPPLEMENTARY MATERIAL

The three Neural Network PESs, in fortran programs, and the photodissociation cross section obtained for the ground vibrational state obtained in this work are supplied in the Supplementary information, giving detailed information about how to be used.

X. ACKNOWLEDGEMENTS

The research leading to these results has received funding from MICIN (Spain) under grants PID2021-122549NB-C21, PID2021-122549NB-C22 and PID2019-106110GB-I00. We thank the PDRs4All-JWST-ERS team for their work in planning, obtaining, and calibrating the spectroscopic observations that led to the detection of interstellar CH_3^+.

XI. DATA AVAILABILITY STATEMENT

The data that support the findings of this study are available from the corresponding author upon reasonable request.

Appendix A: Projecting up spurious solutions

We describe here a method to eliminate spurious states that appear when using fdiscrete variable representation (DVR) and a sequential transformation to the finite basis representation (FBR) to evaluate the angular kinetic terms.

Spherical harmonics, $|j, m\rangle$, form a complete FBR set, and are non-direct products of functions in θ (normalized associated Legendre polynomials depending on the m projection) and ϕ. The transformation to a DVR in θ and ϕ coordinates[68], formed by direct products of Gauss-Legendre points in θ and equispaced points in ϕ, is usually done in consecutive steps to reduce computational effort as[70,71]

$$\langle j, m|\Psi\rangle \leftrightarrow \langle\theta_i, m|\Psi\rangle \leftrightarrow \langle\theta_i, \phi_k|\Psi\rangle, \tag{A1}$$

where ϕ_k are equispaced points in the $[0, 2\pi]$ and θ_i are Gauss-Legendre points in the $[0, \pi]$ interval, used for all projections m. In the intermediate $|\theta_i, m\rangle$ representation m-independent Gauss-Legendre grid of points is not complete for all θ_i values because at the extreme values the associated Legendre polynomials tends to zero as $\sin^m\theta$. We can define a m-dependent closure relationship in a finite FBR and DVR representation as

$$\langle\theta_i|\mathbb{1}^m|\theta_i\rangle = \sum_{j=m}^{j_{max}} \langle\theta_i|j, m\rangle\langle j, m|\theta_i\rangle, \tag{A2}$$

and a graphical representation is shown in Fig. 10.

Clearly, for θ_k near 0 and π the closure relation is far from unity as m increases, and this introduces some spurious states using finite grids/basis. When using the DVR-FBR transformation to evaluate rotational kinetic energy, these spurious states will tend to have zero energy and look like spikes. To remove these states in the physical window of the bound state or wave packet propagation, these states are shifted up in energy by using the projector $\mathcal{P}_m = \mathbb{1}^0 - \mathbb{1}^m$. To do so, once the wave

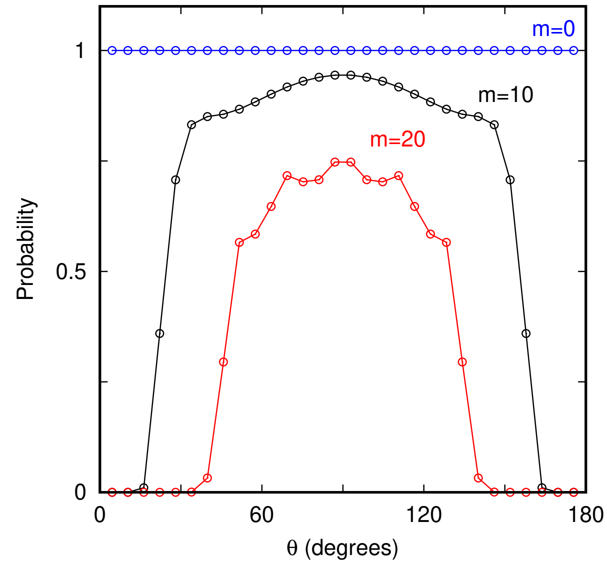

FIG. 10: Closure represented in a grid as $\langle\theta_i|\mathbb{1}^m|\theta_i\rangle$, for m=0, 10 and 20, for j_{max}=29 and a Gauss-Legendre grid of 30 points.

function is expressed in the intermediate representation as $\langle\theta_i, m|\Psi\rangle$, the action of the rotational operator $\mathbf{j}^2$ takes the form

$$\begin{aligned}
&\sum_{i'}\langle\theta_i, m|\mathbf{j}^2|\theta_{i'}, m\rangle\langle\theta_{i'}, m|\Psi\rangle = \qquad\qquad (A3)\\
&= \sum_{j=m}\langle\theta_i, m|j, m\rangle j(j+1)\sum_{i'}\langle j, m|\theta_{i'}m\rangle\langle\theta_{i'}, m|\Psi\rangle\\
&+ \sum_{j=0}\langle\theta_i, 0|j, 0\rangle C_{max}\sum_{i'}\langle j, 0|\theta_{i'}, 0\rangle\langle\theta_{i'}, m|\Psi\rangle\\
&- \sum_{j=m}\langle\theta_i, m|j, m\rangle C_{max}\sum_{i'}\langle j, m|\theta_{i'}, m\rangle\langle\theta_{i'}, m|\Psi\rangle
\end{aligned}$$

where C_{max} is a high positive constant, and here is chosen as the highest value of the potential energy. The three terms in the previous equation are evaluated as successive multiplication of a matrix and a vector, to save computation time.

To illustrate the problem and the solution of this problem in Fig. 11 the mono-dimensional eigenfunctions for θ_1 are shown, which are obtained with and without the projection technique to push up the spurious solutions for different m-values, the projection of $\mathbf{j}_1$ in the body-fixed frame. For m=0, no difference is found. For $m = 10$, the first eigen-function is spurious and it disappears when the projection up technique is applied. For m=20 the situation is even worse, and at least five spurious states appears, which are corrected and pushed up. This problem is very notorious when calculating bound states, because the lower eigen values are mainly spurious. In wave packet propagations, this problem is in the angular representation of the Hamiltonian, and it becomes less evident, but this problem is a source of inaccuracies.

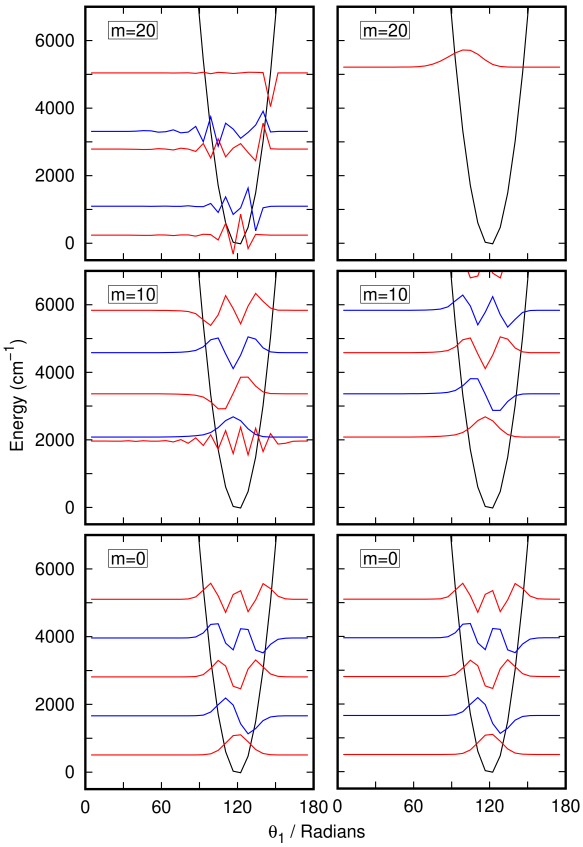

FIG. 11: Monodimensional wave functions in θ_1, keeping the remaining degrees of freedom at its equilibrium values, for $m=0$ (bottom) , $m=10$ (middle) and $m=20$ (top) for the diagonalization in the angular grid without (left panels) and with (right panels) projection up technique. Black lines represent the potential energy, while blue/red are the angular eigen functions shifted to the energy of the eigen value. In this case a Gauss-Legendre angular grid of 30 points is used.

REFERENCES

[1] O. Berné, M.-A. Martin-Drumel, I. Schroetter, and *et al.*, Nature **621**, 56 (2023).
[2] S. Gärtner, J. Krieg, A. Klemann, O. Asvany, S. Brünken, and S. Schlemmer, J. Phys. Chem. A **112**, 9975 (2013).
[3] P. Jusko, A. Stoffels, S. Thorwirthi, S. Brünken, S. Schlemmer, and O. Asvany, J. Mol. Spectroscopy **332**, 59 (2017).
[4] M. Töpfer, T. Salomon, H. Kohguchi, O. Dopfer, K. M. T. Yamada, S. Schlemmer, and O. Asvany, Phys. Rev. Lett. **121**, 143001 (2018).
[5] E. Roueff, M. Guerin, D. C. Lis, A. Wootten, N. Marcelino, J. Cernicharo, and B. Tercero, J. Phys. Chem. A **117**, 9959 (2013).
[6] M. Gerin, D. A. Neufeld, and J. R. Goicoechea, Ann. Rev. Astron. Astrophys. **54**, 181 (2016).
[7] G. K. S. Prakash and P. v. R. Schleyer, *Stable carbocation chemistry* (John Wiley and Sons, New York, 1997).
[8] G. A. Olah and G. K. S. Orakash, *Carbocation chemistry* (John Wiley and Sons, Hoboken, 2004).
[9] M. W. Crofton, M.-F. Jagod, B. D. Rehfuss, W. A. Kreiner, and T. Oka, J. Chem. Phys. **88**, 666 (1988).
[10] M. Jagod, M. Rösslein, M.-F. Gabrys, D. D. Rehfuss, F. Scappini, M. W. Crofton, and T. Oka, J. Chem. Phys. **97**, 7111 (1992).
[11] E. T. White, J. Tang, and T. Oka, Science **284**, 135 (1999).
[12] H. Wang, C. Neese, C. Morong, M. Kleshcheva, and T. Oka, J. Phys. Chem. A **117**, 9908 (2013).
[13] D. Gerlich, R. Disch, and S. Scherbarth, J. Chem. Phys. **87**, 350 (1987).
[14] P. M. Hierl, R. A. Morris, and A. A. Viggiano, J. Chem. Phys. **106**, 10145 (1997).
[15] A. G. G. M. Tielens and D. Hollenbach, AstroPhys. J. **291**, 722 (1985).
[16] A. Sternberg and A. Dalgarno, AstroPhys. J. Suppl. **99**, 565 (1995).
[17] M. Agúndez, J. R. Goicoechea, J. Cernicharo, A. Faure, and E. Roueff, AstroPhys. J. , 662 (2010).
[18] K. F. Kaplan, H. L. Dinerstein, H. Oh, G. N. Mace, H. Kim, K. R. Sokal, M. D. Pavel, S. Lee, S. Pak, C. Park, J. Sok Oh, and D. T. Jaffe, AstroPhys. J. **838**, 152 (2017).
[19] K. F. Kaplan, H. L. Dinerstein, H. Kim, and D. T. Jaffe, AstroPhys. J. **919**, 27 (2021).
[20] A. Zanchet, B. Godard, N. Bulut, O. Roncero, P. Halvick, and J. Cernicharo, ApJ **766**, 80 (2013).
[21] A. Faure, P. Halvick, T. Stoecklin, P. Honvault, E. Epe, J. Z. Mezei, O. Motapon, I. F. Schneider, J. Tennyson, O. Roncero, N. Bulut, and A. Zanchet, Mon. Not. Royal Astronm. Soc. **469**, 612 (2017).
[22] D. Smith, N. G. Adams, and E. Alge, J. Chem. Phys. **77**, 1261 (1982).
[23] O. Asvanay, S. Schlemmer, and D. Gerlich, AstroPhys. J. **617**, 685 (2004).
[24] O. Asvany, S. Thorwirth, B. Redlich, and S. Schlemmer, J. Mol. Spectroscopy , 1 (2018).
[25] R. Signorell and F. Merkt, J. Chem. Phys. **110**, 2309 (1999).
[26] H. J. Wörner, R. van der Veen, and F. Merkt, Phys. Rev. Lett. **97**, 173003 (2006).
[27] P. Asvany, I. Savic, S. Schlemmer, and D. Gerlich, Chem. Phys. **298**, 97 (2004).
[28] P. R. Schreiner, S.-J. Kim, H. F. S. III, and P. von Rague Schleyer, J. Chem. Phys. **99**, 3716 (1993).
[29] O. Asvany, K. M. T. Yamada, S. Brünken, A. Potapov, and S. Schlemmer, Science **347**, 1346 (2015).
[30] A. Dalgarno, in *Proceedings of the Advanced Research Workshop, Bad Windsheim, West Germany, July 8-14, 1984 (A86-39726 18-90)*, edited by G. H. F. Dierksen, W. F. Huebner, and P. W. Langhoff (Dordretch: Springer Netherlands, 1985) p. 3.

[31]V. Wakelam, I. Smith, E. Herbst, J. Troe, W. Geppert, H. Linnartz, K. Öberg, E. Roueff, M. Agúndez, P. Pernot, H. M. Cuppen, J. C. Loison, and D. Talbi, Space Science Rev. **156**, 13 (2010).
[32]M. Chabot, T. IdBarkach, K. Béroff, F. L. Petit, and V. Wakelam, Astron. AstroPhys. **640**, 115 (2020).
[33]T. Henning, I. Kamp, M. Samland, A. M. Arabhavi, J. Kanwar, E. F. van Dishoeck, M. Guedel, P.-O. Lagage, C. Waelkens, A. Abergel, O. Absil, D. Barrado, A. Boccaletti, J. Bouwman, A. C. o. Garatti, V. Geers, A. M. Glauser, F. Lahuis, C. Nehme, G. Olofsson, E. Pantin, T. P. Ray, B. Vandenbussche, L. B. F. M. Waters, G. Wright, V. Christiaens, R. Franceschi, D. Gasman, R. Guadarrama, H. Jang, M. Morales-Calderon, N. Pawellek, G. Perotti, D. Rodgers-Lee, J. Schreiber, K. Schwarz, B. Tabone, M. Temmink, M. Vlasblom, L. Colina, T. R. Greve, and G. Oestlin, arXiv e-prints , arXiv:2403.09210 (2024), arXiv:2403.09210 [astro-ph.EP].
[34]W. P. Kraemer and V. Spirko, J. Mol. Spectroscopy **149**, 235 (1991).
[35]H.-G. Yu and T. J. Sears, J. Chem. Phys. **117**, 666 (2002).
[36]G. Nyman and H.-G. Yu, AIP advances **9**, 095017 (2019).
[37]Changala, P. B., Chen, N. L., Le, H. L., Gans, B., Steenbakkers, K., Salomon, T., Bonah, L., Schroetter, I., Canin, A., Martin-Drumel, M.-A., Jacovella, U., Dartois, E., Boyé-Péronne, S., Alcaraz, C., Asvany, O., Brünken, S., Thorwirth, S., Schlemmer, S., Goicoechea, J. R., Rouillé, G., Sidhu, A., Chown, R., Van De Putte, D., Trahin, B., Alarcón, F., Berné, O., Habart, E., and Peeters, E., Astron. AstroPhys. **680**, A19 (2023).
[38]M. W. Crofton, W. A. Kreiner, M.-F. Jagod, B. D. Rehfuss, and T. Oka, J. Chem. Phys. **83**, 3702 (1985).
[39]J. A. Blush, P. Chen, R. T. Wiedmann, and M. G. White, J. Chem. Phys. **98**, 3557 (1993).
[40]R. T. Wiedmann, M. G. White, K. Wang, and V. McKoy, J. Chem. Phys. **100**, 4738 (1994).
[41]X. Liu, R. L. Gross, and A. G. Suits, Science **294**, 2527 (2001).
[42]A. M. Schulenburg, C. Alcaraz, G. Grassi, and F. Merkt, J. Chem. Phys. **125**, 104310 (2006).
[43]C. A. Taatjes, D. L. Osborn, T. M. Selby, G. Meloni, H. Fan, and S. T. Pratt, J. Phys. Chem. A **112**, 9336 (2008).
[44]J.-C. Loison, J. Phys. Chem. A **114**, 6515 (2010).
[45]B. K. Cunha de Miranda and C. Alcaraz and M. Elhanine and B. Noller and P. Hemberger and I. Fischer and G. A. Garcia and H. Soldi-Lose and B. Gans and L. A. Vieira Mendes and S. Boyé-Péronne and S. Douin and J. Zabka and P. Botschwina, J. Phys. Chem. A **114**, 4818 (2010).
[46]B. Gans and L. A. Vieira Mendes and S. Boyé-Pérone and S. Douin and G. García and H. Soldi-Lose and B. Cunha de Miranda anid C. Alcaraz and N. Carrasco and P. Pernot and D. Gauyacq, J. Phys. Chem. A **114**, 3237 (2010).
[47]A. N. Heays, A. D. Bosman, and E. F. van Dishoeck, Astron. AstroPhys. **602**, A105 (2017).
[48]R. J. Blint, R. F. Marshall, and W. D. Watson, AstroPhys. J. **206**, 627 (1976).
[49]A. Tielens, *The Physics and Chemistry of the Interstellar Medium* (Cambridge University Press, 2010).
[50]H. J. Werner and P. J. Knowles, J. Chem. Phys. **89**, 5803 (1988).
[51]T. Shiozaki and H.-J. Werner, J. Chem. Phys. **134**, 184104 (2011).
[52]H.-J. Werner, P. J. Knowles, G. Knizia, F. R. Manby, and M. Schütz, WIREs Comput Mol Sci **2**, 242 (2012).
[53]J. Hill, S. Maxumder, and K. Peterson, J.Chem. Phys. **132**, 054108 (2010).
[54]M. Delsaut, *Methyl Cation in Astrochemistry: ab initio study of its formation*, Ph.D. thesis, Faculté des Sciences, Université Libre de Bruxelles, (2015).
[55]K. Shao, J. Chen, Z. Zhao, and D. H. Zhang, Journal of Chemical Physics **145**, 071101 (2016).
[56]"Github repository with fi definitions," `https://github.com/pablomazo/FI`, accessed: 2024-01-09.
[57]P. del Mazo-Sevillano, A. Aguado, and O. Roncero, The Journal of Chemical Physics **154**, 094305 (2021).
[58]P. del Mazo-Sevillano, D. Félix-González, A. Aguado, C. Sanz-Sanz, D. Kwon, and O. Roncero, Mol. Phys. , e2183071 (2023).
[59]A. Paszke, S. Gross, F. Massa, A. Lerer, J. Bradbury, G. Chanan, T. Killeen, Z. Lin, N. Gimelshein, L. Antiga, A. Desmaison, A. Kopf, E. Yang, Z. DeVito, M. Raison, A. Tejani, S. Chilamkurthy, B. Steiner, L. Fang, J. Bai, and S. Chintala, in *Advances in Neural Information Processing Systems 32*, edited by H. Wallach, H. Larochelle, A. Beygelzimer, F. d'Alché Buc, E. Fox, and R. Garnett (Curran Associates, Inc., 2019) pp. 8024–8035.
[60]D. C. Liu and J. Nocedal, Mathematical Programming **45**, 503 (1989).
[61]H.-G. Yu and J. T. Muckerman, J. Mol. Spectroscopy , 11 (2002).
[62]J. Cullum and R. Willoughby, *Lanczos Algorithms for Large Symmetric Eigenvalues Computations* (Birkhäuser, Boston, 1985).
[63]C.-E. Fröberg, *Numerical Mathematics: Theory and Computer Applications* (The Benjamin/Cummings Publishing Company, 1985).
[64]R. E. Wyatt, Adv. Chem. Phys. **LXXIII**, 231 (1989).
[65]F. T. Smith, Phys. Rev. Lett. **45**, 1157 (1980).
[66]R. Zare, *Angular Momentum* (John Wiley and Sons, Inc., 1988).
[67]D. T. Colbert and W. H. Miller, J. Chem. Phys. **96**, 1982 (1992).
[68]G. C. Corey and D. Lemoine, J. Chem. Phys. **97**, 4115 (1992).
[69]G. C. Corey, J. W. Tromp, and D. Lemoine, in *Numerical grid methods and their application to Schrödinger equation*, edited by C. Cerjan (Kluwer Academic Publishers, 1993) p. 1.

[70]E. M. Goldfield, Comp. Phys. Comm. **128**, 178 (2000).
[71]S. Y. Lin and H. Guo, J. Chem. Phys. **117**, 5183 (2002).
[72]R. C. Mowrey, J. Chem. Phys. **94**, 7098 (1991).
[73]Y. Guan, H. Guo, and D. R. Yarkony, Journal of Chemical Theory and Computation **16**, 302 (2020), https://doi.org/10.1021/acs.jctc.9b00898.
[74]G. Herzberg and H. C. Longuet-Higgins, Discuss. Faraday **35**, 77 (1963).
[75]M. V. Berry, Proc. R. Soc. Lond. **A392**, 4557 (1984).
[76]C. Xie, D. R. Yarkony, and H. Guo, Phys. Rev. A **95**, 022104 (2017).
[77]V. A. Mandelshtam and H. S. Taylor, J. Chem. Phys. **102**, 7390 (1995).
[78]R. Chen and H. Guo, J. Chem. Phys. **105**, 3569 (1996).
[79]S. K. Gray and G. G. Balint-Kurti, J. Chem. Phys. **108**, 950 (1998).
[80]T. González-Lezana, A. Aguado, M. Paniagua, and O. Roncero, J. Chem. Phys. **123**, 194309 (2005).
[81]M. Paniagua, A. Aguado, M. Lara, and O. Roncero, J. Chem. Phys. **111**, 6712 (1999).
[82]A. Aguado, M. Paniagua, C. Sanz-Sanz, and O. Roncero, J. Chem. Phys. **119**, 10088 (2003).
[83]A. Chenel, O. Roncero, A. Aguado, M. Agúndez, and J. Cernicharo, J. Chem. Phys. **144**, 144306 (2016).
[84]Draine, AstroPhysical J. **37**, 595 (1978).
[85]F. Le Petit, C. Nehmé, J. Le Bourlot, and E. Roueff, Astrophys. J. **164**, 506 (2006), astro-ph/0602150.
[86]J. R. Goicoechea and J. Le Bourlot, Astronomy Astrophys. **467**, 1 (2007), astro-ph/0702033.
[87]J. R. Goicoechea, J. Pety, S. Cuadrado, J. Cernicharo, E. Chapillon, A. Fuente, M. Gerin, C. Joblin, N. Marcelino, and P. Pilleri, Nature **537**, 207 (2016), arXiv:1608.06173.